QUANTUM MATERIALS

Photonic crystals for nano-light in moiré graphene superlattices

S. S. Sunku[1,2], G. X. Ni[1], B. Y. Jiang[3], H. Yoo[4], A. Sternbach[1], A. S. McLeod[1], T. Stauber[5], L. Xiong[1], T. Taniguchi[6], K. Watanabe[6], P. Kim[4], M. M. Fogler[3], D. N. Basov[1]*

Graphene is an atomically thin plasmonic medium that supports highly confined plasmon polaritons, or nano-light, with very low loss. Electronic properties of graphene can be drastically altered when it is laid upon another graphene layer, resulting in a moiré superlattice. The relative twist angle between the two layers is a key tuning parameter of the interlayer coupling in thus-obtained twisted bilayer graphene (TBG). We studied the propagation of plasmon polaritons in TBG by infrared nano-imaging. We discovered that the atomic reconstruction occurring at small twist angles transforms the TBG into a natural plasmon photonic crystal for propagating nano-light. This discovery points to a pathway for controlling nano-light by exploiting quantum properties of graphene and other atomically layered van der Waals materials, eliminating the need for arduous top-down nanofabrication.

When light of wavelength λ_0 travels through media with periodic variations of the refractive index, one witnesses an assortment of optical phenomena categorized under the notion of a photonic crystal (*1*). The additional periodicity imposed on light can trigger the formation of a full photonic bandgap (*2*) and may also produce chiral one-dimensional (1D) edge states (*3*) or exotic photonic dispersions emulating those of Dirac and Weyl quasiparticles (*4*). In principle, the photonic crystal concept is also applicable for controlling the propagation of "nano-light": coupled oscillations of photons and electrons confined to the surface of the conducting medium and referred to as surface plasmon polaritons (SPPs) (*5*–*7*). The wavelength of SPPs, λ_p, is reduced compared with λ_0 by up to three orders of magnitude (*8*). However, this virtuous confinement poses challenges for the implementation of the nano-light photonic crystals by standard top-down techniques (*9*, *10*). In this study, we demonstrate a lithography-free photonic crystal for plasmons in twisted bilayer graphene (TBG). Periodic variations in the optical response of these van der Waals heterostructures arise naturally because of modification of the electronic structures at moiré domain walls (solitons) formed in rotationally misaligned graphene layers (Fig. 1B). The most important feature of the modified electron dispersion is the appearance of chiral 1D states (one pair per valley) (Fig. 1C), which are known to be topologically protected (*11*). The optical transitions involving these 1D states (arrow in Fig. 1C) produce an enhancement of the local optical conductivity across the solitons (*11*). A characteristic profile of the attendant near-field signal is displayed in Fig. 1D and will be discussed below. By using infrared (IR) nano-imaging experiments (Fig. 1A), we visualize the interference between SPPs propagating in solitonic networks and predict the formation of a full plasmonic bandgap.

Graphene has emerged as an extremely capable plasmonic medium in view of ultrastrong confinement, quantified by $\lambda_0/\lambda_p \geq 1000$ (*8*), attained in the regime of weak loss (*12*, *13*). The plasmonic properties of graphene can be readily controlled by the carrier density (*6*, *7*), the dielectric environment (*12*, *14*), and ultrafast optical pulses (*15*). In this study, we have explored and exploited yet another control route based on the twist angle θ between neighboring graphene layers (*14*, *16*–*20*). In TBG, the local stacking order changes smoothly across the narrow solitons separating AB from BA domains (*21*), as revealed (Fig. 1B) by dark-field transmission electron microscopy (TEM). Previous nano-IR experiments on isolated solitons in Bernal-stacked bilayer graphene (BLG) have shown that SPPs in BLG are scattered by the solitons (*11*, *22*), analogous to the scattering of SPPs by grain boundaries in monolayer graphene (*23*). Therefore, a regular pattern of such solitons (Fig. 1B) is expected to act as a periodic array of scatterers, thus fulfilling the key precondition for a nano-light photonic crystal. Unlike all previous implementations of photonic crystals (*24*, *25*), our approach exploits local changes in the electronic band structure of the plasmonic medium, a quantum effect, to control optical phenomena. We explored this novel and fundamentally quantum approach for manipulating plasmons via direct nano-imaging experiments, modeling, and theory.

IR nano-imaging (Fig. 1A) is central to unveiling the physics of a quantum photonic crystal for plasmons. In our experiments, IR light at frequency $\omega = 1/\lambda_0$ is focused on the apex of a metallic tip. The amplitude of the backscattered signal $s(\omega)$ and its phase $\phi(\omega)$ are recorded by using an interferometric detection method (*26*). When ω is close to the optical phonon of the SiO_2 substrate, as in Fig. 1B, IR nano-imaging effectively reveals local variations of the optical conductivity (*26*, *27*). In Fig. 1B, we observed a sixfold pattern of bright line-like features with even stronger contrast at the intersections. A dark-field TEM image of a similar TBG sample also reveals the same sixfold symmetry with features matching the nano-IR data. The periods of both patterns are consistent with the moiré length scales anticipated for a nominal twist angle of ~ 0.1°. An accurate estimate of the periodicity a for our device can be directly read off the near-field image: Given the observed a = 230 nm, we obtain a twist angle of $\theta = 0.06°$ (*26*). We therefore conclude that the near-field image constitutes a direct visualization of the solitonic lattice.

The nano-IR contrast at the solitons is the result of topological changes to the electronic structure. When inversion symmetry is broken by an application of a perpendicular displacement field using the back gate, the Bernal-stacked AB and BA domains open a bandgap (*28*) and the valley Chern number at K and K' valleys is ±1 (*29*). As the stacking order reverses across the soliton, the Chern numbers also change sign. The difference in Chern number leads to topologically protected 1D states along the soliton (*30*, *31*). The key implication of this band structure effect (*11*) is that optical transitions from the topologically protected states to empty states above the Fermi level prompt an enhanced conductivity at the soliton (Fig. 1C). Consistent with this view, resistivity experiments signal ballistic electron transport along the solitonic channels (*17*, *32*).

Our qualitative understanding of the near-field contrast is corroborated by modeling. The near-field amplitude and phase profiles $s_{sol}(x)$ and $\phi_{sol}(x)$, where x is the coordinate normal to the soliton, depend on the Fermi energy μ, the interlayer bias V_i, and the plasmonic damping rate η [section S4 of (*26*)]. These latter profiles obtained for isolated solitons (*11*, *22*) were fully elucidated by combining electronic structure calculations, scattering theory, and numerical modeling of the tip-sample coupling (*11*, *33*). Figure 1D shows $s_{sol}(x)$ calculated by using parameters that most closely correspond to the experiment in Fig. 1B.

We now discuss the effect of periodic soliton networks in TBG on propagating plasmon polaritons. In our experiments, SPPs of wavelength λ_p of the order of the soliton periodicity a are introduced by the metallic tip (Fig. 1A) (*12*, *15*). To launch propagating polaritons, we choose ω to be away from phonon resonances. In this regime, the scattering of SPPs by the solitons

[1]Department of Physics, Columbia University, New York, NY 10027, USA. [2]Department of Applied Physics and Applied Mathematics, Columbia University, New York, NY 10027, USA. [3]Department of Physics, University of California–San Diego, La Jolla, CA 92093, USA. [4]Department of Physics, Harvard University, Cambridge, MA 02138, USA. [5]Departamento de Teoría y Simulación de Materiales, Instituto de Ciencia de Materiales de Madrid, CSIC, E-28049 Madrid, Spain. [6]National Institute for Materials Science, Namiki 1-1, Tsukuba, Ibaraki 305-0044, Japan.
*Corresponding author. Email: db3056@columbia.edu

produces fringes in both $s(\omega)$ (*6*, *7*) and $\phi(\omega)$ (*34*) corresponding to standing waves. 2D maps of both observables are displayed in Fig. 2. We obtained these images in different regimes of λ_p/a by tuning the gate voltage V_G and/or λ_0. All images are dominated by maxima and minima in the nano-IR contrast, indicating the presence of constructive and destructive interference of SPPs triggered by the solitonic lattice.

The Fourier analysis of the $s(\omega)$ images shown in Fig. 3, A and B, supports our conjecture of a photonic crystal. We denote the magnitude of the 2D spatial Fourier transform of the $s(\omega)$ image as $\tilde{s}(q)$. Figure 3A shows $\tilde{s}(q)$ extracted from the spatially varying conductivity image displayed in Fig. 1B and is seen to have sixfold rotational symmetry. This symmetry is preserved in the $\tilde{s}(q)$ images obtained by transforming data in

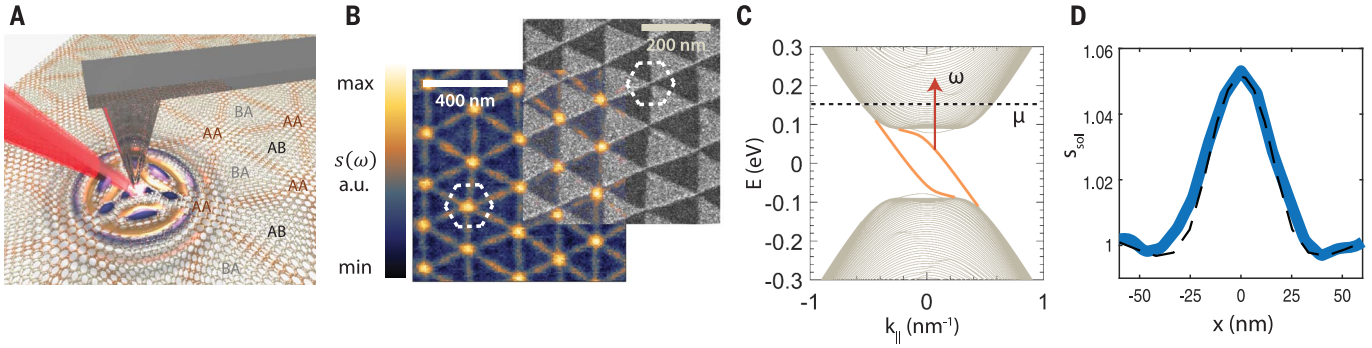

Fig. 1. Nano-light photonic crystal formed by a network of solitons in TBG. (**A**) Schematic of the IR nano-imaging experimental setup. AB, BA, and AA label periodically occurring stacking types of graphene layers. (**B**) (Left) Visualizing the nano-light photonic crystal formed by the soliton lattice. The contrast is due to enhanced local optical conductivity at solitons. (Right) Dark-field TEM image of a TBG sample showing contrast between AB and BA triangular domains. The dashed hexagons represent unit cells of the crystals. a.u., arbitrary units. (**C**) Electronic band structure of a single infinitely long soliton (only the *K* valley is shown). Chiral 1D states are depicted in orange. Optical transitions such as those indicated by the arrow are responsible for the enhanced local conductivity at the location of solitons. E, energy; $k_{||}$, momentum along the soliton. (**D**) Experimental (solid) and calculated (dashed) near-field signal $s_{sol}(x)$ across a single soliton line. Calculation parameters are frequency ω = 1180 cm^{-1}, Fermi energy μ = 0.3 eV, interlayer bias V_i = 0.2 V, and dimensionless damping η = 0.2.

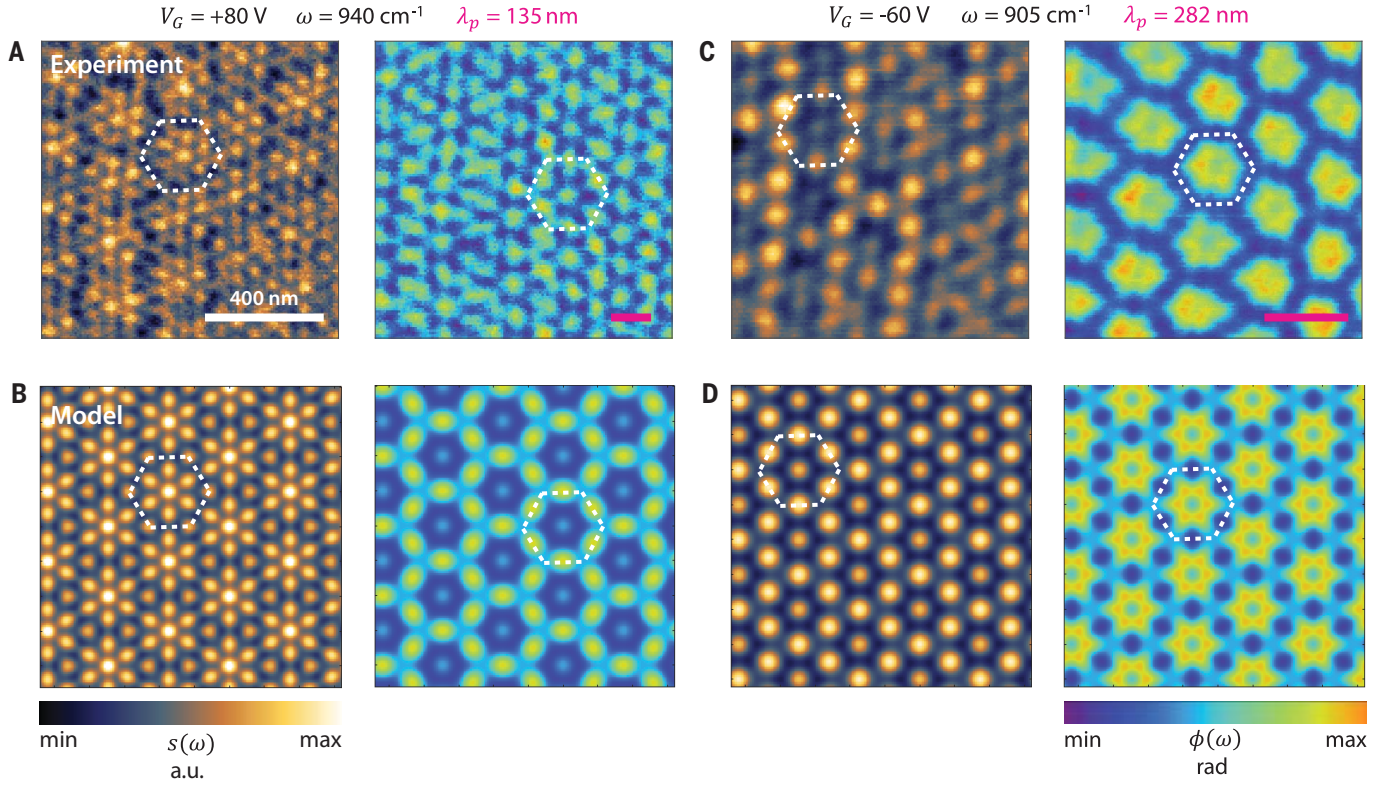

Fig. 2. Plasmon interference patterns and superposition model analysis. (**A** and **C**) Nano-IR images obtained for λ_p = 135 nm and 282 nm. (**B** and **D**) Near-field amplitude and phase images calculated using the superposition model (introduced in the text). The model parameters used to obtain the images are (B) μ = 0.23 eV, V_i = 0.3 V, and η = 0.2 and (D) μ = 0.35 eV, V_i = 0.1 V, and η = 0.2. The dashed hexagons represent the boundaries of a single unit cell, and the magenta bars represent the SPP wavelengths.

Fig. 2 in the regime where our structures support propagating SPPs. Figure 3B shows the line profiles taken along one of the high-symmetry directions for all $\tilde{s}(q)$ images. The peaks in all the line profiles are anchored at the same momenta in Fourier space, indicating that the periodicity of the polaritonic nano-IR patterns matches that of the moiré lattice. Our nano-IR imaging and its Fourier-transformed patterns thus give further evidence of plasmonic interference in the soliton crystal formed in TBG.

For a quantitative analysis of the SPP interference, we introduce a superposition model. In this simplified model, we neglect multiple scattering of plasmons by these domain walls and disregard any interaction of the domain walls at their intersections. In other words, we treat the domain walls as interpenetrating and decoupled objects. We compute the near-field signal produced by a single (infinitely long) soliton via microscopic calculations of the electron band structure, optical conductivity, and tip-sample coupling (*11*, *33*). The superposition model takes as a basic input the profiles of the near-field amplitude $s_{sol}(x)$ and phase $\phi_{sol}(x)$ [Fig. 1D and section S4 of (*26*)] for a single soliton. It is easy to see that the 2D soliton lattice consists of three 1D periodic arrays rotated in-plane by 120° with respect to one another. Consider one such array with solitons located at equidistant positions x_k. Within the superposition model, this array produces the complex near-field signal equal to the sum $\sum_k s_{sol}(x - x_k)e^{i\phi_{sol}(x-x_k)}$. Since $s_{sol}(x)$ is rapidly decreasing away from the solitons, it is sufficient to keep only a few nearest-neighbor terms in this summation. The signal from the remaining 1D arrays is calculated in a similar way. The superposition of all these signals yields the images displayed in Fig. 2, B and D. This procedure yields a close correspondence between the experimental data and the model in both amplitude and phase.

A key feature of moiré photonic crystal is its tunability. The periodicity a of the crystal can be continuously varied by changing the twist angle (*17*), and the SPP-soliton scattering strength can be modulated by the carrier density and the interlayer bias (*11*). To illustrate the tunability, we introduce the dimensionless scattering strength

$$t = \frac{1}{a}\int_{-\infty}^{\infty} dx \frac{\sigma_s(x) - \sigma_0}{\sigma_0} \quad (1)$$

that governs the interaction between the SPPs and the solitons. Here, $\sigma_s(x)$ is the local IR conductivity along the direction perpendicular to the soliton, and σ_0 is the asymptotic value of this conductivity far away from the soliton (*11*, *33*). Parameter t governs the long-range behavior of the SPP waves scattered by a soliton. The details of the short-range behavior (an example of which is shown in Figs. 1D and 2, B and D) depend, in general, on the exact profile $\sigma_s(x)$. However, the plasmon band structure is predominantly sensitive to the long-range processes, so a single parameter t suffices. We now evaluate the plasmonic band structure in momentum space for selected t values by using a reciprocal-space method (*26*, *35*). Figure 3C shows the band structure for parameters that correspond most closely to our current experiment (a = 230 nm, t = 0.02); we notice that the plasmonic gap is insignificant. However, a larger scattering strength that is likely to be attained in future experiments does yield a full bandgap, arresting plasmonic propagation (Fig. 3E). We also note that a point-like source in plain graphene launches an isotropic cylindrical wave (Fig. 3D, left) whose amplitude decays asymptotically as the square root of the distance. Although the decay is expected to be the same for a plasmonic crystal at frequencies within the plasmonic bands, the rotational

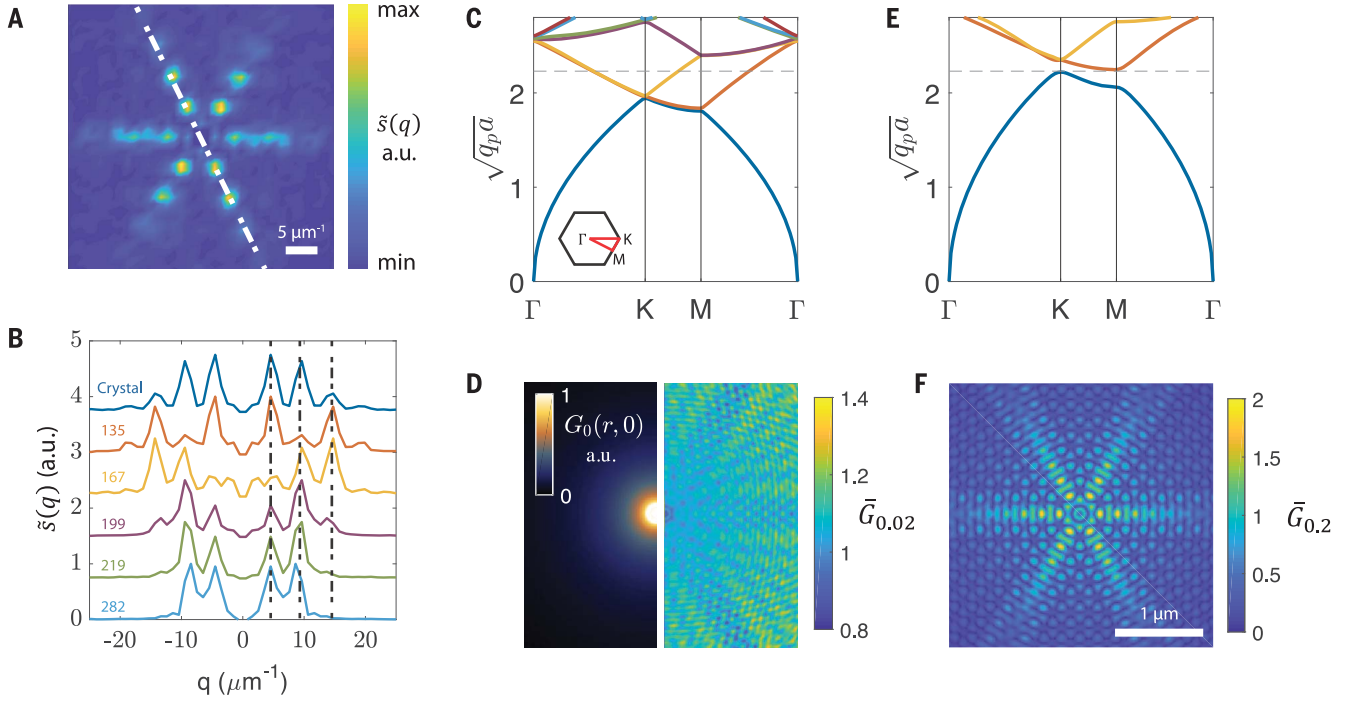

Fig. 3. Properties of the graphene-based quantum photonic crystal. (**A**) Fourier transform $\tilde{s}(q)$ of the photonic crystal image with no propagating SPPs (as in Fig. 1B). (**B**) Line profiles of $\tilde{s}(q)$ taken along the dashed line in (A) for the crystal devoid of propagating SPPs and for the same crystal with propagating SPPs of various wavelengths λ_p. The curves are vertically offset for clarity. (**C**) Plasmonic band structure for dimensionless scattering strength t = 0.02, defined in the text; t = 0.02 most closely corresponds to the experimentally studied crystal. Γ, K, and M are high-symmetry points in the Brillouin zone, as indicated in the inset. (**D**) Near-field signal calculated for a point source at an AA vertex. (Left) G_0, the near-field signal computed for the empty lattice (t = 0). r, spatial coordinate. (Right) The ratio $\bar{G}_{0.02} = G_{0.02}/G_0$, where $G_{0.02}$ is the signal for t = 0.02. (**E**) Plasmonic band structure for t = 0.2 showing the formation of a full plasmonic gap. (**F**) Near-field signal ratio $\bar{G}_{0.2} = G_{0.2}/G_0$, where $G_{0.2}$ is the signal for t = 0.2. The frequency in both (D) and (F) corresponds to the plasmon momentum q_p that satisfies $\sqrt{q_p a} = 2.23$, shown by the dashed lines in (C) and (E). When this frequency is outside (inside) the bandgap, the plasmonic patterns are delocalized (localized) and weakly (strongly) anisotropic; compare (D) [(F)]. See section 7 of (*26*) for details of these calculations.

symmetry of the waves must reduce to comply with the symmetry of the crystal. The reduction to sixfold symmetry for our crystal can be revealed by dividing the signals with and without the crystal pointwise (Fig. 3D, right). By contrast, excitations at frequencies inside the bandgap must be localized, showing exponential decay of the amplitude away from the source. We also predict that the localized states are strongly anisotropic, yielding signal distributions resembling snowflakes (Fig. 3F) or three-pointed stars [Fig. 1A and (*26*)]. To generate patterns of this kind, one can add point-like plasmonic emitters, such as small gold disks (*36*), to the system.

The nano-light photonic crystal devised, implemented, and investigated in this work is distinct in a number of ways. First, the local variation of the response is rooted in topological electronic phenomena occurring at the solitons, at variance with commonplace classical photonic crystals based on locally perforated media. Second, its key parameters (periodicity and band structure) can be continuously tuned electrostatically and/or nanomechanically (*37*) and do not require challenging top-down fabrication. It would be of interest to explore the regime close to the charge neutrality, where the solitons are predicted to host 1D plasmon modes (*11*, *38*). In this regime, our structure would act as a 2D network or possibly as a controllable circuit capable of routing such 1D plasmons.

REFERENCES AND NOTES

1. J. D. Joannopoulos, S. G. Johnson, J. N. Winn, R. Meade, *Photonic Crystals: Molding the Flow of Light* (Princeton Univ., 2008).
2. L. Lu, J. D. Joannopoulos, M. Soljačić, *Nat. Photonics* **8**, 821–829 (2014).
3. Z. Wang, Y. Chong, J. D. Joannopoulos, M. Soljacić, *Nature* **461**, 772–775 (2009).
4. L. Lu *et al*., *Science* **349**, 622–624 (2015).
5. D. N. Basov, M. M. Fogler, F. J. García de Abajo, *Science* **354**, aag1992 (2016).
6. Z. Fei *et al*., *Nature* **487**, 82–85 (2012).
7. J. Chen *et al*., *Nature* **487**, 77–81 (2012).
8. D. Alcaraz Iranzo *et al*., *Science* **360**, 291–295 (2018).
9. D. Jin *et al*., *Phys. Rev. Lett.* **118**, 245301 (2017).
10. M. Jung, Z. Fan, G. Shvets, *Phys. Rev. Lett.* **121**, 086807 (2018).
11. B. Y. Jiang *et al*., *Nano Lett.* **17**, 7080–7085 (2017).
12. A. Woessner *et al*., *Nat. Mater.* **14**, 421–425 (2015).
13. G. X. Ni *et al*., *Nature* **557**, 530–533 (2018).
14. G. X. Ni *et al*., *Nat. Mater.* **14**, 1217–1222 (2015).
15. G. X. Ni *et al*., *Nat. Photonics* **10**, 244–247 (2016).
16. C. R. Woods *et al*., *Nat. Phys.* **10**, 451–456 (2014).
17. H. Yoo *et al*., arXiv:1804.03806 [cond-mat.mtrl.-sci] (2 October 2018).
18. Z. Fei *et al*., *Nano Lett.* **15**, 4973–4978 (2015).
19. F. Hu *et al*., *Phys. Rev. Lett.* **119**, 247402 (2017).
20. S. Huang *et al*., *Phys. Rev. Lett.* **121**, 037702 (2018).
21. J. S. Alden *et al*., *Proc. Natl. Acad. Sci. U.S.A.* **110**, 11256–11260 (2013).
22. L. Jiang *et al*., *Nat. Mater.* **15**, 840–844 (2016).
23. Z. Fei *et al*., *Nat. Nanotechnol.* **8**, 821–825 (2013).
24. A. Drezet *et al*., *Nano Lett.* **7**, 1697–1700 (2007).
25. A. M. Lakhani, M. K. Kim, E. K. Lau, M. C. Wu, *Opt. Express* **19**, 18237–18245 (2011).
26. Materials and methods are available as supplementary materials.
27. Z. Fei *et al*., *Nano Lett.* **11**, 4701–4705 (2011).
28. Y. Zhang *et al*., *Nature* **459**, 820–823 (2009).
29. F. Zhang, A. H. MacDonald, E. J. Mele, *Proc. Natl. Acad. Sci. U.S.A.* **110**, 10546–10551 (2013).
30. I. Martin, Y. M. Blanter, A. F. Morpurgo, *Phys. Rev. Lett.* **100**, 036804 (2008).
31. Z. Qiao, J. Jung, Q. Niu, A. H. Macdonald, *Nano Lett.* **11**, 3453–3459 (2011).
32. L. Ju *et al*., *Nature* **520**, 650–655 (2015).
33. B. Y. Jiang *et al*., *Phys. Rev. Lett.* **117**, 086801 (2016).
34. J. A. Gerber, S. Berweger, B. T. O'Callahan, M. B. Raschke, *Phys. Rev. Lett.* **113**, 055502 (2014).
35. I. Silveiro, A. Manjavacas, S. Thongrattanasiri, F. J. García De Abajo, *New J. Phys.* **15**, 033042 (2013).
36. S. Dai *et al*., *Nano Lett.* **17**, 5285–5290 (2017).
37. R. Ribeiro-Palau *et al*., *Science* **361**, 690–693 (2018).
38. E. H. Hasdeo, J. C. W. Song, *Nano Lett.* **17**, 7252–7257 (2017).

ACKNOWLEDGMENTS

Funding: Research on topological properties of moiré superlattices is supported as part of Programmable Quantum Materials, an Energy Frontier Research Center funded by the U.S. Department of Energy (DOE), Office of Science, Basic Energy Sciences (BES), under award DE-SC0019443. Research in topological phenomena in graphene is supported by DOE, BES, under award DE-SC0018426. Work on photonic crystals is supported by ONR-N000014-18-1-2722. Work on self-assembled photonic structures is funded by DARPA EXTREME program award HR001110720034. Development of nano-optics instrumentation is supported by AFOSR: FA9550-15-1-0478 and DOE-BES DE-SC0018218. D.N.B. and P.K. are Gordon and Betty Moore Foundation investigators in the Quantum Materials EPIQS program under GBMF4533 and GBMF4543. P.K. acknowledges support from ARO (W911NF-17-1-0574) and ONR MURI (N00014-15-1-2761). T.S. acknowledges additional funding from the Ministerio de Economia y Competitividad, Spain (FIS2017-82260-P). K.W. and T.T. acknowledge support from the Elemental Strategy Initiative conducted by the MEXT, Japan, and the CREST (JPMJCR15F3), JST. **Author contributions:** All authors were involved in designing the research, performing the research, and writing the paper. **Competing interests:** The authors declare no competing financial interests. **Data and materials availability:** All data are available in the main text or the supplementary materials.

SUPPLEMENTARY MATERIALS

www.sciencemag.org/content/362/6419/1153/suppl/DC1
Materials and Methods
Supplementary Text
Figs. S1 to S9
References (*39*–*46*)

29 July 2018; accepted 29 October 2018
10.1126/science.aau5144

Photonic crystals for nano-light in moiré graphene superlattices

S. S. Sunku, G. X. Ni, B. Y. Jiang, H. Yoo, A. Sternbach, A. S. McLeod, T. Stauber, L. Xiong, T. Taniguchi, K. Watanabe, P. Kim, M. M. Fogler and D. N. Basov

Science **362** (6419), 1153-1156.
DOI: 10.1126/science.aau5144

Twisting a route for surface plasmons

Graphene is an atomically thin material that supports highly confined plasmon polaritons, or nano-light, with very low loss. The properties of graphene can be made richer by introducing and then rotating a second layer so that there is a slight angle between the atomic registry. Sunku *et al.* show that the moiré patterns that result from such twisted bilayer graphene also provide confined conducting channels that can be used for the directed propagation of surface plasmons. Controlling the structure thereby provides a pathway to control and route surface plasmons for a nanophotonic platform.

Science, this issue p. 1153